Synthesis of V_2AlC thin films by thermal annealing of nanoscale elemental multilayered precursors: incorporation of layered Ar bubbles and impact on microstructure formation

Chongchong Tang[a*], Michael Dürrschnabel[a], Ute Jäntsch[a], Michael Klimenkov[a], Martin Steinbrück[a], Sven Ulrich[a], Marcus Hans[b], Jochen M. Schneider[b], Michael Stüber[a]

[a] Institute for Applied Materials (IAM-AWP), Karlsruhe Institute of Technology (KIT), D-76021 Karlsruhe, Germany

[b] Materials Chemistry, RWTH Aachen University, D-52074 Aachen, Germany

* Corresponding author

Email: chongchong.tang@kit.edu

Abstract

Periodically stacked nanoscale V/C/Al multilayered thin film precursors were deposited by magnetron sputtering using elemental targets. Their temperature-dependent phase transformation during subsequent thermal annealing in argon towards V_2AlC MAX phase formation was investigated. Compositional and microstructural analyses at the nanoscale revealed undulation growth of the nanolayers and preferential incorporation of Ar atoms into amorphous carbon nanolayers within the as-deposited multilayered precursors. Single-phase and basal-plane-oriented V_2AlC films were formed at annealing temperatures above 560°C. The incorporated Ar atoms migrated and aggregated into high-density nanoscale Ar clusters/bubbles located essentially at grain boundaries after annealing, displaying pronounced layered distribution characteristics especially adjacent to the substrate/film interface. The heterogeneous incorporation of argon atoms or clusters in heterostructured films composed of multicomponent sublayers likely represents a common phenomenon during thin film nucleation and growth, while its impact on the macroscopic properties of films remains to be explored.

Keywords: MAX phase; physical vapor deposition (PVD); nanoscale multilayers; phase transformations; atom probe tomography (APT)

1. Introduction

$M_{n+1}AX_n$ phases (MAX phases, M: transition metal, A: mainly A-group element, X: carbon or nitrogen, n: typically 1-3) are a class of intrinsically nanolaminated ternary compounds [1]. These nanolaminated compounds possess unusual and remarkable properties combining attributes of both metals and ceramics that stem from their unique layered structure and bonding characteristics. More specifically, their crystal structures comprise twinned $M_{n+1}X_n$ slabs of edge-sharing M_6X octahedrons interleaved with atomic layers of the A element, with strong covalent-ionic M-X bonds and relatively weak metallic M-A bonds. Considerable pioneering work has been done on the processing and properties characterization of sintered bulk MAX phase materials [1,2]. In parallel, there has been tremendous and continuously increasing interest in synthesizing MAX phase thin films and coatings for applications in surface engineering [3,4].

Thin-film synthesis of MAX phase materials has been predominantly carried out by physical vapor deposition (PVD) techniques, such as magnetron sputtering, cathodic arc evaporation, and pulsed laser deposition. The synthesis procedures comprise two main approaches, i.e. (1) direct growth with deliberate heating of substrates, and (2) solid-state reaction synthesis by thermal annealing of as-deposited multilayered or amorphous precursors [3]. Early studies on MAX phase films have focused on the epitaxial growth of MAX phase structures on single crystal substrates and determination of their fundamental properties [5,6]. Intensive efforts are currently underway to optimize procedures for synthesizing high-quality (i.e. single-phase and textured) and relatively thick MAX phase films (at least a few microns) on different types of substrate materials [7–9]. However, their complex chemistry and lattice structures raise difficulties in achieving single-phase MAX phase films on technologically relevant substrates with favorable crystallographic orientation and reduced processing temperature. Our previous studies revealed that phase-pure and basal-plane textured Ti_2AlC and Ti_3AlC_2 films can be readily synthesized by thermal annealing of magnetron-sputtered multilayered thin film precursors with pre-defined nanostructured architectures (i.e. periodical stacking of nanometer-thin layers of the constituent elements) [10,11]. Several further studies demonstrated similarly that using element targets in PVD, following a layer-by-layer approach, offers advantages for precise control of individual element fluxes towards accurate precursor design and for enabling synthesis of high-purity MAX phase thin films [12–14]. For instance, Stevens et al. have grown epitaxial Cr_2AlC MAX phase thin films by sequential layer-by-layer deposition at 600°C using pulsed laser deposition [14].

Among the previously reported MAX phase films synthesized by PVD, V_2AlC was found to require a relatively low processing temperature (~600°C) and possess a fairly low resistivity (30 μΩ·cm), which makes it attractive for various electrical applications [3]. In addition, synthesis of V_2AlC films using multilayered precursors has not been reported yet. This study focuses on synthesis of V_2AlC MAX phase films via thermal annealing of periodically stacked V/C/Al multilayered thin film

precursors deposited by magnetron sputtering using a layer-by-layer approach. The temperature-dependent phase formation of the annealed multilayered precursors was investigated by in-situ high-temperature X-ray diffraction (HT-XTD) and ex-situ XRD. In particular, comprehensive microstructural and compositional analyses at the nanoscale, combining high-resolution scanning transmission electron microscopy (HR-STEM) and atom probe tomography (APT), were performed to gain a deeper understanding of the thermally induced phase formation and microstructural evolution. We observed a preferential incorporation of Ar atoms into amorphous carbon nanolayers within the multilayered thin film precursors. During the annealing process towards V_2AlC MAX phase formation, these Ar atoms migrate and aggregate into nanoscale Ar clusters/bubbles that are distributed in a well-defined, periodically layered arrangement.

2. Experimental

The periodically stacked V/C/Al multilayered thin film precursors were deposited by magnetron sputtering using a Leybold Z 550 coater from three elemental targets, vanadium, graphite, and aluminum. The precursors consist of 60 multilayered stacks with each stack made of approximately 13 nm V/4 nm C/8 nm Al nanolayers, resulting in an overall multilayer thickness of ~1.5 µm. The films were deposited on two different types of substrates, i.e. Si (100) wafer (for compositional analyses) and polished polycrystalline Al_2O_3 (for annealing studies). The chamber was evacuated to a base pressure of ~ 1×10^{-4} Pa. Before deposition, the substrates were sputter cleaned for 15 min in an argon plasma powered with 500 W. The working pressure of Ar was kept at 0.5 Pa and the targets were powered at 200 W (DC for V, and RF for C and Al). The substrates were not intentionally heated and were at ground potential during deposition. To obtain the multilayered structure of the precursors, sequential deposition was performed in a stop-and-go manner during the top-down sputtering process. More specifically, both the substrate holder and the shutter between the target and the substrates were rotated in the deposition chamber to allow deposition of one element at a time. The different sublayer thicknesses were realized by varying the dwell time of the substrates under the respective element target. Details of the multilayer deposition are described in previous works [10,11].

In-situ high-temperature X-ray diffraction (HT-XRD) was performed on films deposited on Al_2O_3 substrates to explicitly investigate their temperature-dependent phase formation during heat treatment. The measurements were carried out in an argon atmosphere with temperature step of 20 K, ranging from 300°C to 1000°C. The samples were heated inside an Anton Paar HTK 1200N (Anton Paar GmbH) chamber with a heating rate of 30 K/min from room temperature to 300°C and between each step. An Empyrean diffractometer (Malvern Panalytical) was used to collect the XRD patterns in Bragg-Brentano geometry (θ-2θ) with a measurement range of 2θ from 10° to 60°. The diffractometer was operated with Cu Kα radiation (λ = 0.1540 nm) of 40 kV and 40 mA, and the measurement time for each pattern was approximately 20 minutes. The multilayered precursors were additionally annealed in the cycling mode in flowing Ar from 400°C to 1000°C with 10 K/min heating rate using a NETZSCH STA-449 F3 Jupiter thermal balance and dwell time of 10 min. An oxygen trapping system with a Zr oxygen getter was used to reduce the residual oxygen content in the system to avoid considerable oxidation of the films. The overall composition of the as-deposited precursors were measured by electron probe microanalysis (EPMA, JEOL JXA-8530F). Microstructural and compositional analyses of an as-deposited and an 800°C annealed thin film precursor were carried out by high-resolution scanning transmission electron microscopy (HR-STEM, Thermofisher Talos F200X) operating at 200 kV. The lamellas for TEM analyses were prepared by the focused ion beam technique and thinned by Ga ion milling at 30 kV. The 3D chemical composition at the nanometer scale of an as-deposited as well as a thin film precursor after annealing at 800°C has been further studied by atom probe tomography (APT, CAMECA LEAP 4000X HR). Specimen preparation was done employing focused ion beam techniques in a dual-beam microscope (FEI Helios Nanolab 660) according to a standard protocol [15]. As the film-substrate interface region was of interest, the remaining film thickness was checked by STEM imaging of the APT specimen within the same dual-beam microscope and low voltage cleaning (5 kV) was carried out until the remaining film thickness was < 300 nm. The final remaining film thickness was used as input for the atom probe reconstruction. Field evaporation was assisted by thermal pulsing using 50 pJ laser pulse energy, 125 kHz laser pulse frequency, 60 K base temperature and the detection rate was set at 0.5%.

3. Results

The average elemental composition of the as-deposited multilayers measured by EPMA was: V 50.5 at.%, Al 24.5 at.%, C 21.8 at.%, including O 2.9 at.% and Ar 0.3 at.% as impurities. Considering only V, Al, and C, the composition of the multilayered thin film precursors coincides well with the nominal stoichiometry of V_2AlC except for a slight sub-stoichiometry in carbon concentration. Furthermore, the impurity oxygen level may be overestimated due to the overlap of the K-shell transition of O-K (0.525 keV) with the L-shell transition of V-L (0.511 keV).

Fig. 1 (a) and (b) show the diffraction patterns of as-deposited and up to 1000°C annealed thin film precursors obtained from in-situ HT-XRD and ex-situ XRD after cyclical annealing, respectively. In the as-deposited multilayers, the transition metal (V) nanolayers grow in nanocrystalline structure and exhibit a preferred orientation with a broad diffraction peak of the V (110) lattice plane. Diffraction signals from Al and C nanolayers cannot be clearly resolved due to their very low thickness and with respect of the amorphous character of the carbon layers. In the HT-XRD patterns, the V (110) reflection gradually shifts to lower diffraction angles and becomes more asymmetric, with increasing annealing temperature from 300 to ~420°C. These observations suggest that aluminum and carbon atoms diffuse preferentially into the vanadium nanolayers at low annealing temperature because of their higher mobility. A very broad, low-intensity reflection centered at ~40° appeared at an annealing temperature around 440°C, which does not change significantly up to ~500°C. Based on previous studies [16,17], this specific reflection can be assigned to the (002) lattice plane of a pre-ordering solid solution $(VAl)_2C_x$ carbide phase. At 560°C annealing, a pronounced while broad reflection appears around a diffraction angle of 41.1°, and a second reflection at low diffraction angle ~ 13.2° can be seen. Both reflections are indicative of the growth of the V_2AlC MAX phase (PDF card #29-0101). Upon annealing to 800°C, these reflections show an increased intensity and are getting more symmetric in shape, while shifting moderately to lower diffraction angles due to thermal expansion. The diffraction intensity attributed to the V_2AlC MAX phase reached a maximum at ~800°C during HT-XRD measurements and then declined progressively, accompanied by the appearance of signals from V-O oxides (VO, V_3O_4 and finally V_2O_3) with further increasing temperatures. There are few unindexed diffraction peaks in Fig. 1(a), exhibiting a relative integrated intensity fraction of < 10%. Those peaks located at ~29.9° and 36.8°, observed at an annealing temperature of 800°C, can be assigned to the formation of vanadium oxide, VO (PDF card #15-0629). The peaks located at ~30.9°, 34.0° and 37.0° are observed for an annealing temperature of 860°C and can be attributed to the formation of V_3O_4 (PDF card #34-0615). They are considered as metastable and intermediate phases occurring prior to further oxidation towards to the formation of higher oxidation state phase (V_2O_3) as a large variety of metastable and stable structures of vanadium oxides exist in the vanadium-oxygen system [18]. The observation of these phases is attributed

to the technically given conditions of the high-temperature annealing, when a lower oxygen residual gas pressure in the chamber cannot be excluded. The appearance of a shoulder peak at ~37.3° at 900°C is assigned to the formation of a vanadium carbide phase, VC_x (PDF card #35-0986), which points to a beginning decomposition of the V_2AlC MAX phase by partial oxidation during the HT-XRD measurements.

The XRD patterns after cyclical annealing agree excellently with the HT-XRD observations at low annealing temperatures up to 600°C, as displayed in Fig.1 (b). However, in the cyclical annealing experiments, no phenomena of the kind described above (reduced diffraction intensity of MAX phase and detection of V-O oxides) were observed for annealing at higher temperatures; the reflections attributed to the V_2AlC progressively narrowed and their intensity increased sharply with increasing annealing temperatures, indicating enhanced crystallinity. These different observations could be ascribed to the relatively higher level of residual oxygen contamination in the HT-XRD chamber and poor oxidation resistance of the V_2AlC MAX phase [19]. Phase-pure V_2AlC films were successfully synthesized after annealing at temperatures of 600°C and above, and the reflections from predominantly V_2AlC (000l) lattice planes indicate the typical basal plane oriented growth of the V_2AlC crystallites.

The average crystallite sizes estimated on basis of the Scherrer equation and the normalized peak intensity of the V_2AlC (0002) reflection after cycling annealing are presented in Fig. 1(c). The estimated crystallite size was in the range of 10 nm for V in the as-deposited multilayers and thus slightly lower than its individual nanolayer thickness (~13 nm). The preferential diffusion of aluminum and carbon into the vanadium nanolayers likely leads to the formation of short-range ordered clusters at 400°C, further reducing its crystallite size. A nanocrystalline, intermediate $(VAl)_2C_x$ carbide phase formed at 500°C, with grains of only a few nanometers. The size of V_2AlC crystallites increases approximately linearly from ~13 nm at 600°C to ~58 nm at 1000°C.

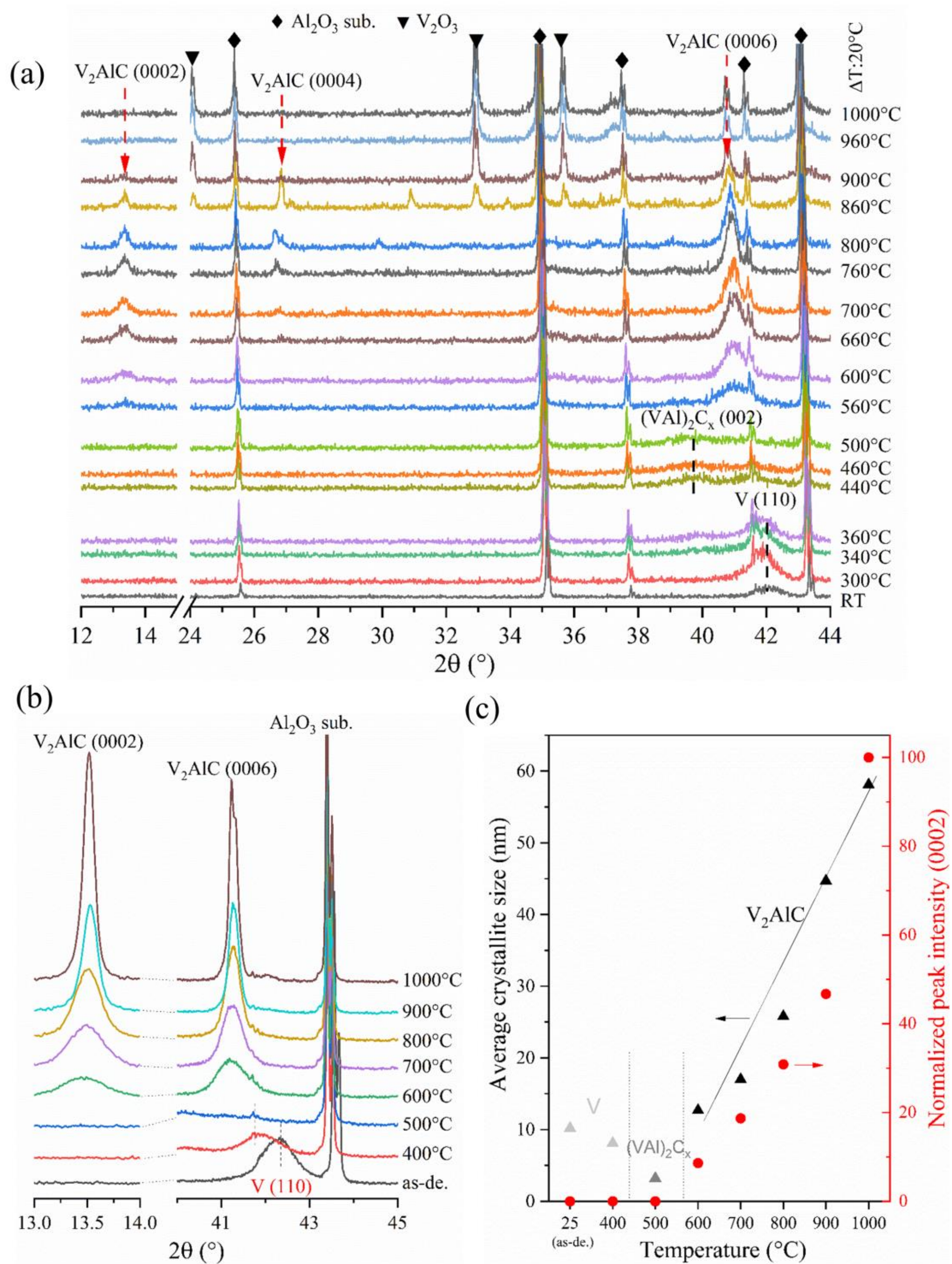

Fig. 1. Temperature-dependent phase evolution of the V/C/Al multilayered thin film precursors on polycrystalline Al_2O_3 substrate identified by in-situ HT-XRD and ex-situ XRD in argon. (a) Selected in-situ HT-XRD patterns of sample annealed from 300 to 1000°C with a temperature step of 20 K. (b) XRD patterns of sample after cycling annealing from 400 to 1000°C with dwell time of 10 min at each temperature. (c) Estimated average crystallite size and normalized peak intensity of V_2AlC (0002) after cycling annealing.

Fig. 2 shows the cross-sectional STEM-HAADF image and EDX mapping of the V/C/Al multilayered precursor in the as-deposited state near the film/substrate interface (more TEM results are available in the supplementary Figs. S1-3). The multilayered thin film precursors with periodically stacked, alternating V/C/Al nanolayers can be clearly resolved by EDX mapping, and the selected area electron diffraction (SAED) pattern confirms the nanocrystalline nature of the V and Al layers (Fig. S1). The thicknesses of the respective elemental nanolayers fit well with the pre-defined values, with a thickness of each trilayer stack of ~25 nm. However, the nanolayers are only perfectly horizontally aligned at the initial first few stacks close to the substrate, and undulation growth (wavy/wrinkle imperfections at nanolayer interfaces) is observed with further deposited stacks. The undulation growth of the nanolayers is progressively augmented from the interface extending to the film surface (Figs. S2 and S3). The upper stacks contain a high density of irregularities, showing higher roughness and even discontinuities of the elemental nanolayers. Apart from the anticipated periodical stacking of principal nanolayers (V, C, and Al), an inhomogeneous distribution of incorporated Ar atoms with an unambiguously layered structure into the as-deposited multilayered precursors was also observed. The incorporated Ar atoms are preferentially enriched in the amorphous C nanolayers and the first layers reveal slightly higher Ar concentrations, as indicated by EDX mapping in Figs. 2 and S2.

Fig. 3 displays the 3D chemical composition analysis of a multilayered precursor adjacent to the film/substrate interface by APT. The preferential incorporation of Ar atoms into amorphous C nanolayers was further confirmed, as revealed by the reconstruction of V, Al, C, O, and Ar atomic positions as well as ≥ 2 at.% Ar isoconcentration surfaces. The first V/C/Al stack on alumina substrate was clearly resolved, and the maximum intensities of C and Ar signals coincide with each other in the chemical composition profiles (Fig. 3(b)) and proximity histograms (Fig. 3 (c)). The concentration of incorporated Ar reaches above 5 at.% within the C nanolayers, while below 0.2 at.% in the Al and V nanolayers.

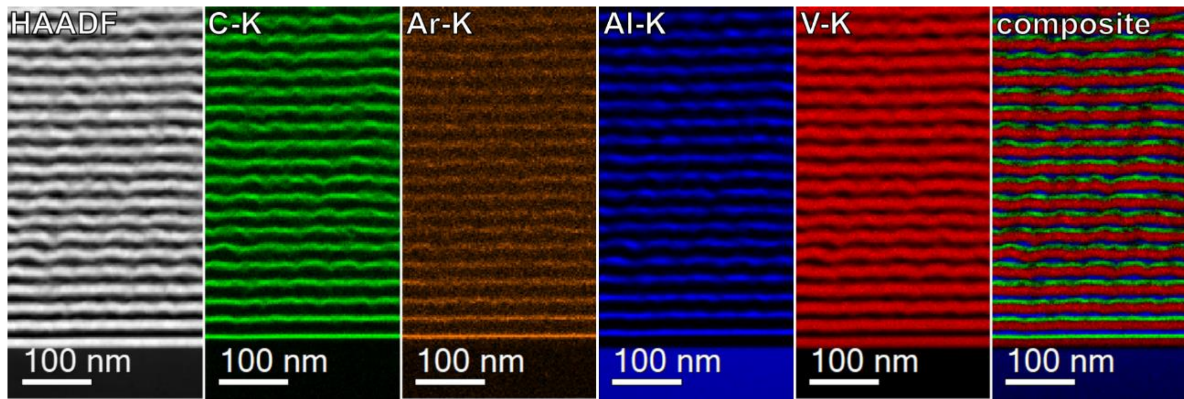

Fig. 2. High-angle annular dark field (HAADF) cross-sectional STEM image and EDX mapping of a V/C/Al multilayered precursor in the as-deposited state at film/substrate interface.

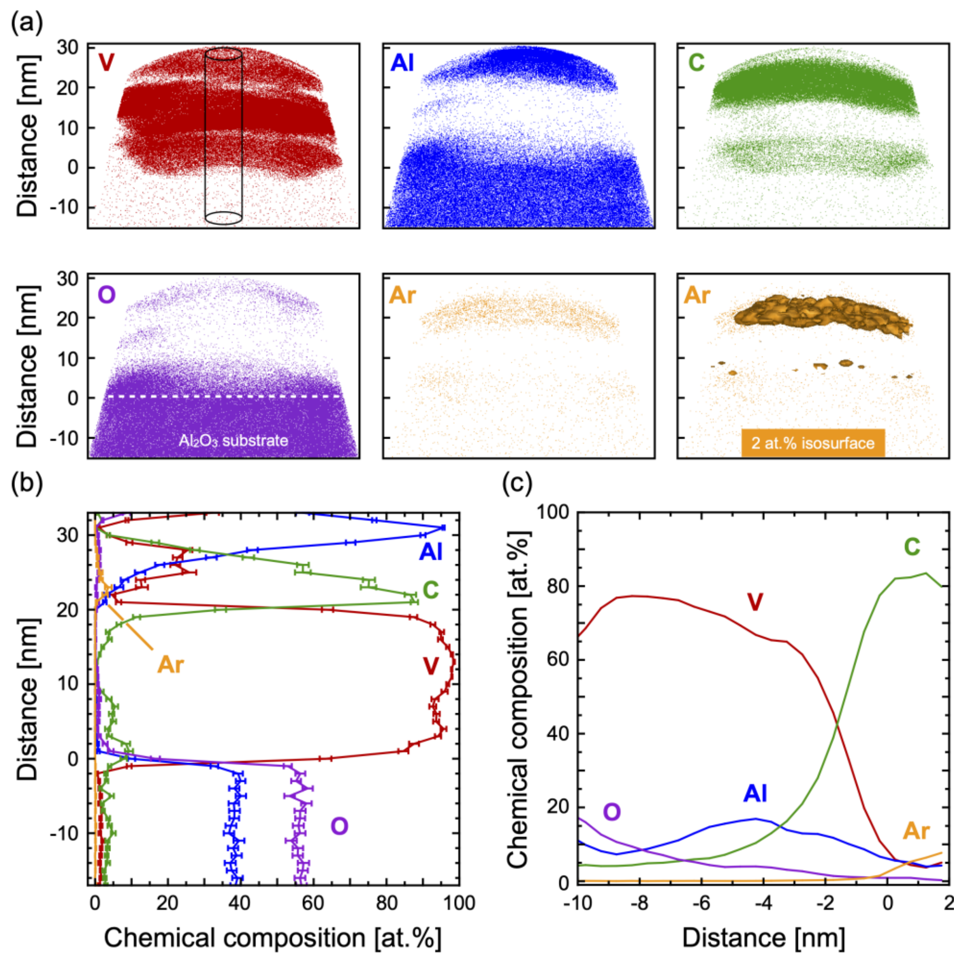

Fig. 3. Local chemical composition analysis of the multilayered precursors adjacent to the film/substrate interface by APT. (a) Reconstruction of V, Al, C, O and Ar atomic positions as well as Ar-rich regions with ≥ 2 at.% are highlighted by isoconcentration surfaces. (b) Chemical composition profile along the cylinder with dimensions of 10 x 10 x 50 nm as indicated in the reconstruction of V atomic positions. (c) Proximity histogram of Ar-rich regions, obtained from isoconcentration surfaces with ≥2 at.% Ar.

Fig. 4 presents results of the TEM analysis of the 800°C annealed precursors on alumina substrate. The cross-sectional bright-field TEM image in Fig. 4 (a) shows that the original multilayered stacks no longer exist and the fully crystallized films exhibit a dense and homogeneous morphology. The SAED pattern superimposed by a simulated ring pattern (based on V_2AlC, PDF card #29-0101) in Fig. 4 (b) displays excellent consistency with existence of the V_2AlC MAX phase. No diffraction signals originating from impurity phases were identified, which confirmed the growth of single-phase V_2AlC grains. The high-resolution HAADF-STEM image illustrated in Fig. 4 (c) reveals that the V_2AlC crystallites are free of typical columnar growth and more horizontally elongated, mainly parallel or slightly inclined to the film/substrate interface. Individual crystallites essentially appear basal-plane oriented and grain boundaries are atomically sharp at (0001)-type lattice planes, which is consistent with the XRD data. The atomic configuration with the unique nanolaminated structure consisting of V_2C layers interleaved with Al layers of the V_2AlC MAX phase can be clearly seen in Fig. 4 (d). Further, nanospherical clusters with different contrast were detected within the film, and some of those are highlighted by red arrows in Fig. 4 (c). They were identified as predominantly nanoscale Ar-rich clusters/bubbles with a few oxygen-rich clusters by subsequent STEM-EDX mapping and APT analyses.

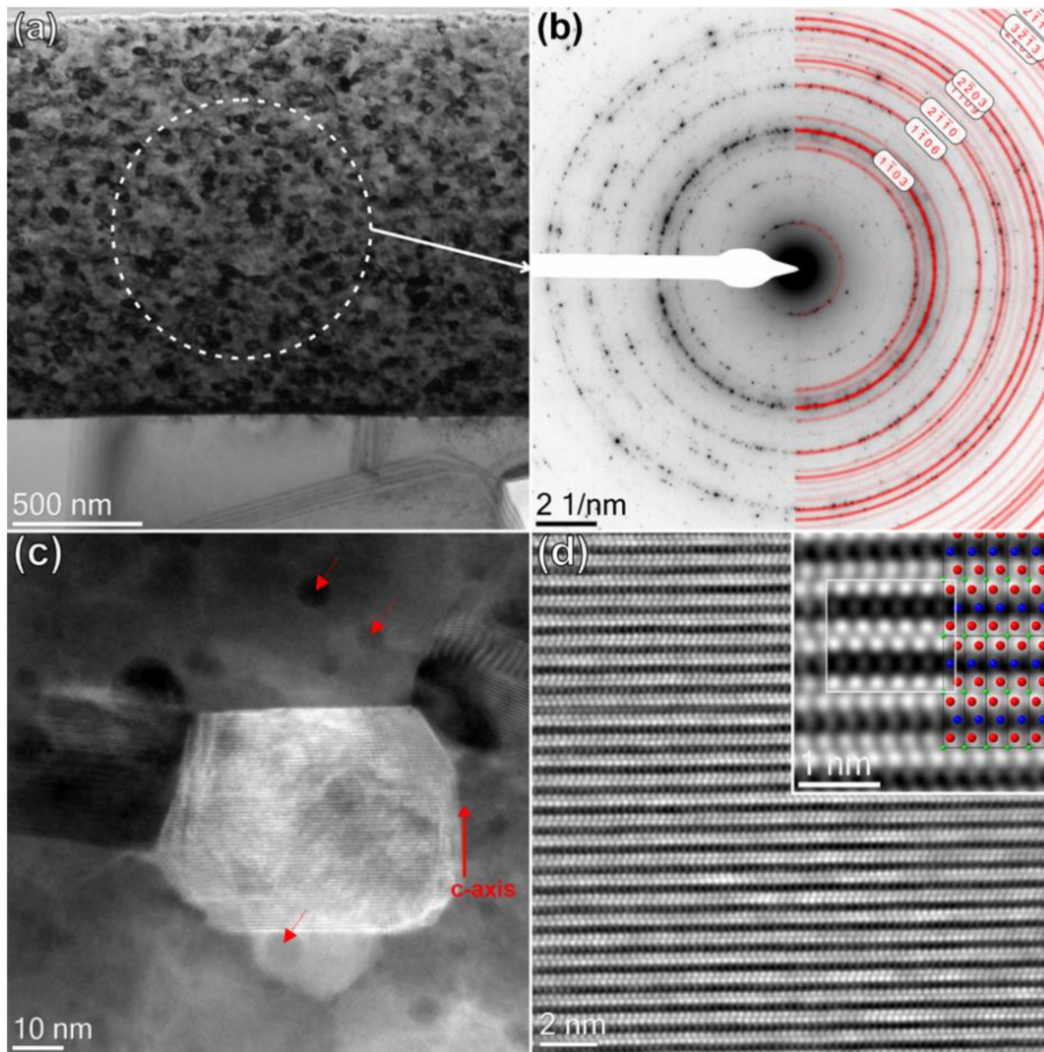

Fig. 4. TEM analysis of V/C/Al multilayered precursors on alumina substrate after annealing at 800°C, 10 min in argon. (a) Cross-sectional bright-field image. (b) SAED pattern, taken from the area marked in (a), superimposed by a simulated ring pattern (generated using SingleCrystal ™). (c) HAADF image of a single V_2AlC grain located in the film center, and the red arrows indicate the spherical Ar clusters/bubbles. (d) Atomic resolution images of the grain center. The inset in (d) shows a magnified view overlaid by a simulated image and an atomic model of V_2AlC in [11-20] zone-axis orientation with red color for V atoms, blue for Al atoms, and green for C atoms.

Fig.5 (a) displays STEM-EDX mapping results over the cross-section of the annealed thin film adjacent to the film/substrate interface, and (b) and (c) are superimposed TEM images with Ar mapping at the film/substrate interface as well as close to the film surface, respectively. The distribution of principal elements (V, C, Al) appears homogeneous within the film at the nanoscale. The distribution of the impurity elements O and Ar reveals heterogeneous features, suggesting the formation of O-rich clusters and nanoscale Ar-rich regions. Oxygen contamination originating from water desorption may migrate to form such O-rich clusters of oxides or

amorphous phases during post-deposition annealing [20]. Further, oxygen incorporation into MAX phase structures, occupying mainly C lattice positions, has been demonstrated for various MAX phase thin films [21,22]. Noticeably, the incorporated Ar atoms that are predominantly enriched in the amorphous C nanolayers within the as-deposited multilayered precursors (Fig. 2) have migrated and aggregated into spherical Ar-rich regions after annealing. These Ar-rich regions expose a distinct layered distribution, parallel to the film/substrate interface and initial nanolayer interfaces (Fig. 5(a)). The superimposed images of Fig. 5(b) and (c) indicate that the layered characteristics of the Ar-rich regions are more pronounced adjacent to the film/substrate interface. The average distance between two layered Ar-rich regions near the film/substrate interface is approximately 25 nm (see Fig. 5(a) of Ar mapping), which is identical to the initial thickness of one V/C/Al stack. The layered features become less noticeable and the distribution of Ar-rich regions appears more random near the surface. A more random distribution of the Ar-rich regions was also seen where the substrate surface contains pore defects (Fig. 5(b)), which interrupt the multilayered structure of the as-deposited precursors near the defect region. The difference is likely due to the enhanced undulation growth of the nanolayers in the surface-near region. In addition, the superimposed images provide evidence that the Ar-rich regions are mainly located at V_2AlC grain boundaries. This is reasonable since segregation of impurities to grain boundaries by diffusion represents a common phenomenon to reduce the (strain) energy of a system [23].

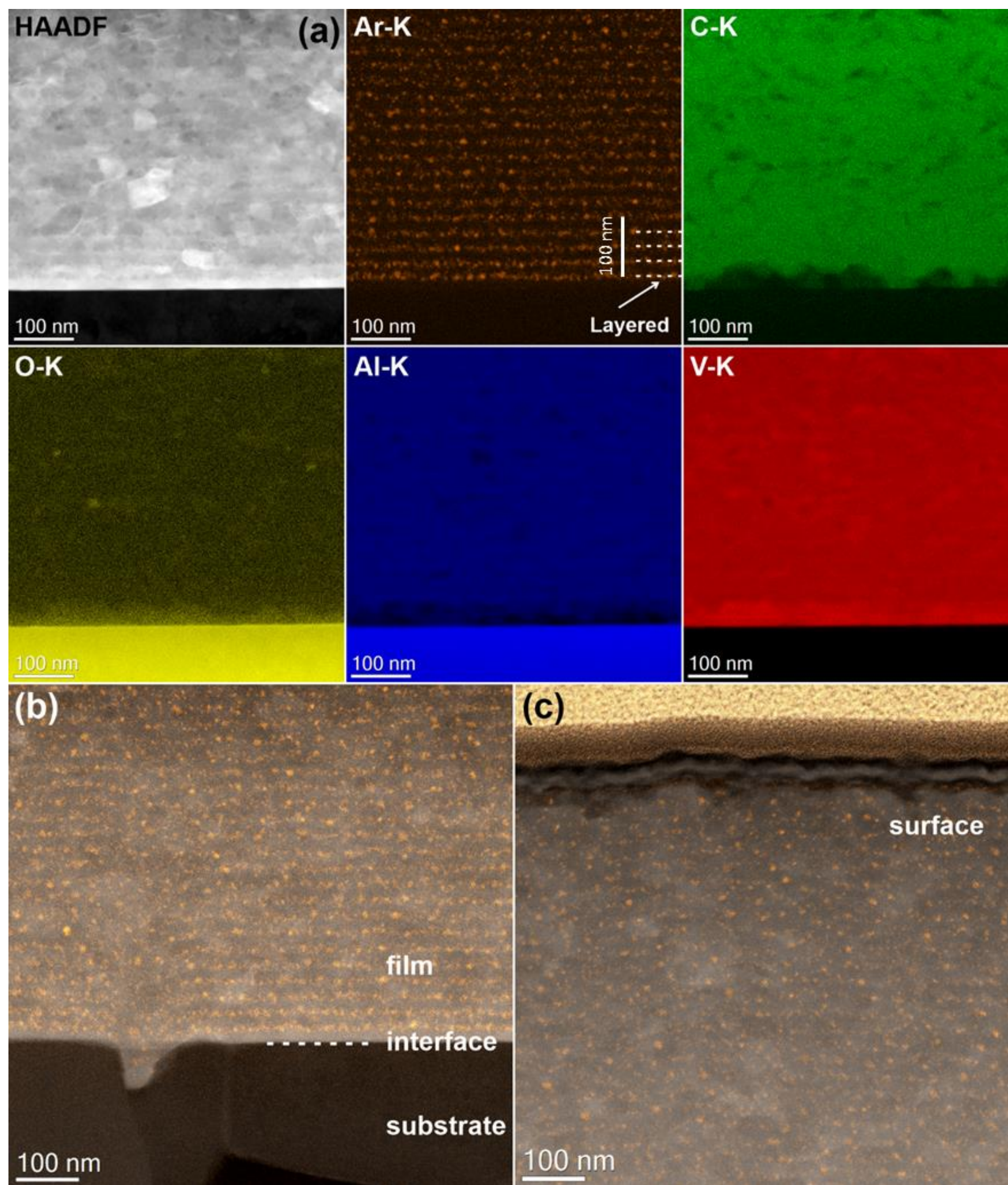

Fig. 5. STEM-EDX mapping of the multilayered precursors on alumina substrate after annealing at 800°C, 10 min in argon. (a) HAADF image with mapping results, and superimposed TEM images with Ar mapping in orange at (b) substrate/film interface and (c) film surface.

Fig. 6 depicts the 3D spatially-resolved compositional analysis at the nanometer scale of the 800°C annealed film by APT. The reconstruction of V, Al, C, O and Ar atomic positions is shown in Fig. 6(a). The chemical composition profile along a cylinder region is presented in Fig. 6(b). The locally higher intensity oxygen signal can be correlated with that of Al and V. It is evident that after high-temperature annealing the O-rich regions exhibit a pronounced Al content, which can be rationalized by the higher oxygen affinity of Al compared to V. The formation of O-rich regions with up to 28 at.% has been also observed for Cr_2AlC films after vacuum annealing at 600°C and explained by residual gas in the vacuum furnace [24]. Moreover, the local formation of VC_x can be inferred from Al depletion in the composition profile at a distance of approximately 70 nm (Fig. 6(b)), as well as from a region close to the film-substrate interface where no Al atoms are detected (Fig. 6(a)). The absence of VC_x diffraction signals in XRD is most probably due to their small size, low volume ratio and plausible amorphous state. The formation of high-density nanoscale Ar-rich regions is obvious, as can be seen from Fig. 6(a). The proximity histogram of regions with concentrations ≥ 2 at.% Ar displayed in Fig. 6(c) reveals that the Ar content increases sharply up to above 50 at.%, which suggests the formation of Ar bubbles as combined with TEM observations. While the absolute size of O- and Ar- rich regions (bubbles) might be affected by the uncertainties of the reconstruction, it can be concluded that the O-rich clusters are larger (~4 ± 2 nm) than the Ar bubbles (~2 ± 1 nm), while their number density is much lower. The Ar bubbles are close to spherical as the radius calculation from volume or area results in similar values with < 20% deviation which is within the uncertainty of the radius values.

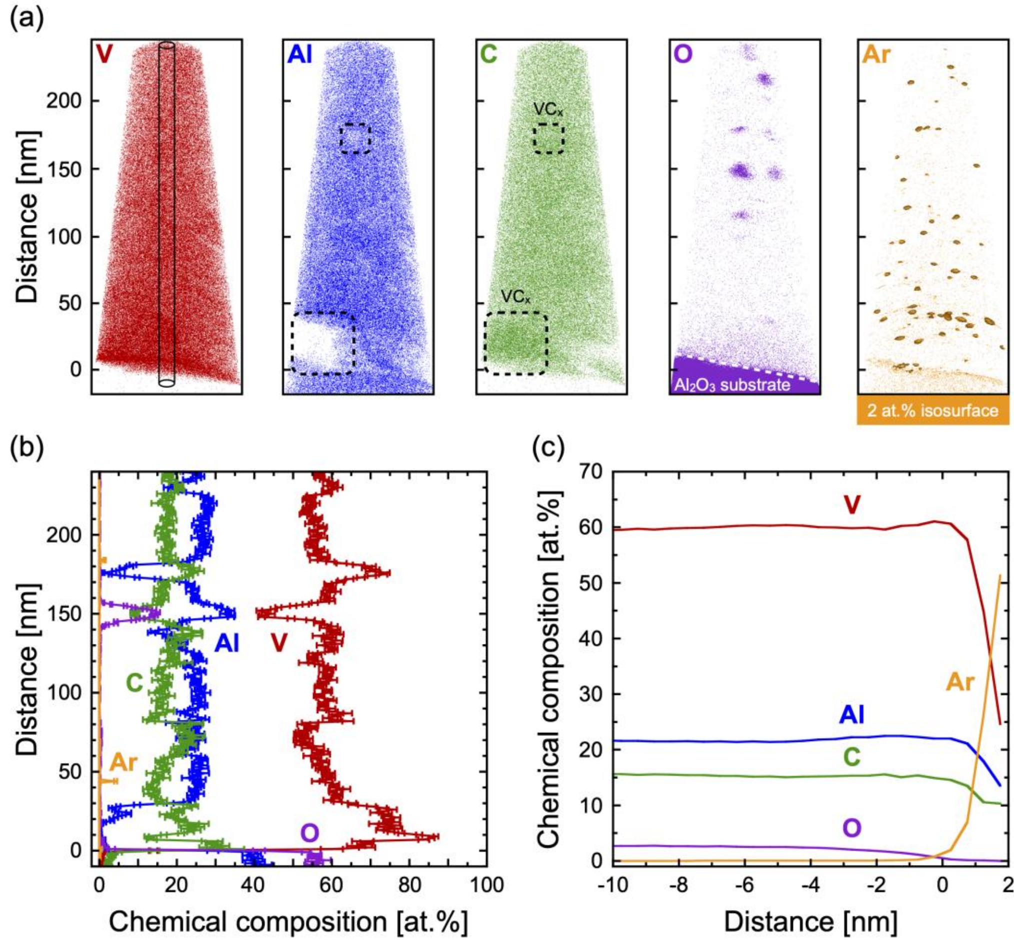

Fig. 6. Local chemical composition analysis of the multilayered precursors adjacent to the film/substrate interface after annealing at 800°C, 10 min in argon by APT. (a) Reconstruction of V, Al, C, O, and Ar atomic positions and Ar-rich regions with ≥ 2 at.% are highlighted by isoconcentration surfaces. (b) Chemical composition profile along the cylinder with dimensions of 10 x 10 x 260 nm as indicated in (a). (c) Proximity histogram of Ar-rich regions, obtained from isoconcentration surfaces with ≥ 2 at.% Ar.

4. Discussion

Thermal annealing of nanostructured elemental multilayer precursors offers a facile, universal strategy to synthesize single-phase MAX phase carbide films by easily adjusting the desired stoichiometry (via the thickness of individual nanolayers) of the precursors and the subsequent thermal processing. This has been demonstrated in this work for MAX phase formation in V/C/Al multilayered precursors and has been shown previously in other systems by various authors [10,13,14]. In addition, the crystallized MAX phase films typically exhibit basal-plane-preferred orientation with elongated crystallites parallel to the film/substrate interface. Highly textured growth of the MAX phase film during thermal annealing can be rationalized by the preferential orientation relationships between initial transition metal nanolayers to intermediate solid solution carbide, and finally MAX phase structures [10], i.e. V(110) // $(VAl)_2C_x$ (002) // V_2AlC (0002) here.

Comprehensive nanostructural investigations reveal undulation growth and preferential incorporation of Ar atoms into amorphous C nanolayers within the multilayered precursors (Figs. 2 and 3). The progressively enhanced undulation growth of the multilayers can be explained by probably two-fold reasons: (1) stress accumulation, and (2) island growth of the subsequently deposited nanolayers. Magnetron-sputtered thin films have often compressive residual stresses with stress gradients that maximize at the film surface [25,26]. It is plausible that the steadily enhanced stress level leads to the deformation of individual nanolayers with wavy interfaces considering their few nanometer thicknesses. In addition, the interfacial lattice mismatches, here fcc Al, bcc V, and amorphous C, will cause various stress levels at the interfaces and enhance the waviness [27]. Transition from the layer-by-layer to island-based (or mixed) growth likely occurs, especially for the V nanolayers, when they are not in contact with the rigid alumina substrate as the deposition progresses (see Figs. 2 and S2), which increases the roughness of the nanolayer interfaces.

Incorporation of Ar atoms from the working gas into sputter-deposited films, including metallic [28,29], ceramic [30,31], and amorphous carbon films [32], have been frequently observed. The trapped Ar atoms originate from two primary sources: reflected energetic Ar atoms and Ar ions that are accelerated to the substrate by an applied substrate bias [30]. The amount of incorporated Ar atoms into the films depends not only on the growth temperature and ion energy, but also on the constituent elements and crystalline quality of the designated film. Fig. 7 compares the content of incorporated Ar in different types of films deposited by sputtering without substrate bias from this work and some previous studies. For instance, Lee et al. investigated the concentration of trapped Ar in 12 different metallic films deposited under similar conditions and found that their argon contents scatter significantly from 0.06 at.% in Al films to as high as 17 at.% in Ta films [28]. Their findings revealed that the energy of reflected Ar atoms

rises as the atomic weight of the target material increases, resulting in a positive correlation between the Ar content and the atomic weight of the metal. However, for elements with low atomic number, e.g., Cu and below, their ability to reflect energetic Ar atoms appears to be weak, and the Ar content in these films varies little (Fig. 7). Schwan et al. reported that ~ 6 at.% of Ar was incorporated into tetrahedral amorphous carbon films deposited using RF sputtering at an argon-ion energy of 24 eV (without substrate bias) [32]. They found that Ar incorporation is restricted as the density of the amorphous carbon film increases. In addition, Chien et al. recently reported that both energy and flux of the reflected Ar rise as the mass of the transition metal in the target increases when sputtering three composite M2AlC (M: Cr, Zr, and Hf) targets, causing pronounced Ar incorporation into the films and preferential re-sputtering of Al in the films [33]. Our present work further demonstrates that substantial different levels of Ar atoms can be incorporated into the sublayers of heterostructured, multilayered films with different types of components, leading to their layered distribution. The crystalline quality likely serves as the decisive factor affecting the magnitude of trapped Ar atoms in films made of relatively light constituent elements. Since Al and V have a smaller atomic number than Cu, it is expected that they may not be highly efficient at reflecting Ar atoms. Furthermore, as shown in Fig. 7, the amount of Ar atoms incorporated into the Al nanolayers and amorphous C nanolayers in this study was of the same order of magnitude as reported by Lee and Oblas for their Al films [28] and reported by Schwan et al. for their amorphous C films [32], respectively. Previously molecular dynamics simulations have suggested that the Ar atoms are preferentially trapped inside the nanovoids within the films [34]. The amorphous C sublayers evidently exhibit lower packing density and higher density of nanovoids compared to the nanocrystalline Al and V sublayers, which leads to more than 20 times higher amounts of trapped Ar atoms compared to the two metallic layers. Since the Ar ions cannot be efficiently reflected by the graphite target, the trapped Ar atoms may essentially originate from a few Ar ions that are attracted to the substrate by a self-bias effect using the RF operation mode [35]. A slightly higher concentration of trapped Ar atoms within the amorphous C nanolayers was observed for initially deposited stacks at the film/substrate interface compared to those in the center/close to the surface (as displayed in Figs. 2 and S2). The variations in Ar concentration maybe be related with the slight substrate temperature increase during deposition and deformation of later deposited elemental nanolayers. Both phenomena can enhance the diffusion and desorption of trapped Ar atoms [31], leading to its somewhat lower concentration within the multilayered stacks in the center/close to the surface. In addition, the high uncertainties of EDX in measuring light elements and the change of the matrix at interface may overestimate such difference in Ar concentration. In general, heterogeneous incorporation of Ar atoms with considerably different levels can be anticipated for multilayered films composed of both crystalline and amorphous phases or made of components with widely different atomic masses.

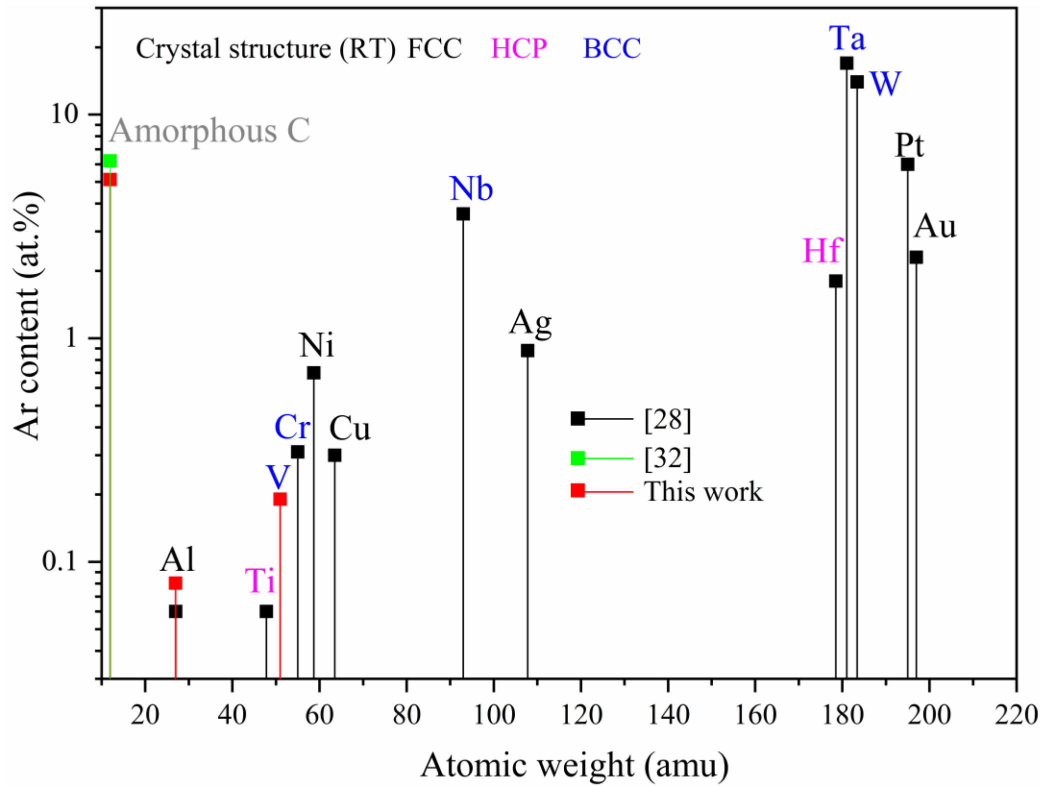

Fig. 7. The content of incorporated Ar in different types of films deposited by sputtering as a function of atomic weight. RT: room temperature, FCC: face-centered cubic HCP: hexagonal close-packed, BCC: body-centered cubic.

Noticeably, thermal annealing provides kinetic energy for the atoms, and the trapped Ar atoms migrate and aggregate into layered structures with nanoscale, locally Ar-enriched regions, with a tendency to form nanoscale Ar bubbles, precipitating primarily at the grain boundaries of the forming MAX phase film during annealing. The layered feature of the precipitated Ar bubbles originates from the originally layered distribution of the Ar atoms and lateral growth of the MAX phase crystallites. The atom diffusion is initially confined in one elemental stack, and the growth of elongated V_2AlC crystallites hinders the rapid coalescence of these Ar bubbles in the vertical direction. Grain boundary segregation with local chemical changes may affect the material's macroscopic properties, such as electric conductivity, fracture toughness, and irradiation behavior, profoundly by orders of magnitude [23,36,37]. Thin films with multilayered structures and various types of components are increasingly designed to achieve superior properties compared to single-layer films [38]. In addition, thin film deposition at low temperatures or assisted by energetic ions (initially gas ions, particularly Ar, and nowadays metal ions have attracted more attention) are increasingly adopted to control the nanostructure and associated properties of deposited films [39]. These ion-assisted deposition processes often lead to significant amounts of Ar incorporation in interstitial sites of the film structure [39]. However,

most studies focus on the energetic ion bombardment on modifying the structure and properties of single-layer thin films. The incorporation behavior and migration characteristics of Ar atoms into the sublayers of multilayered films have not attracted much attention. Understanding the incorporation, migration and precipitation of (layered) Ar atoms/bubbles and their impact on modifying the physical and mechanical properties of multilayered thin films during deposition, post-deposition processing and practical application remain to be explored, and are of great importance for thin-film technology.

5. Conclusions

In conclusion, single-phase and basal-plane-oriented V_2AlC MAX phase films were synthesized by thermal annealing of nanostructured V/C/Al multilayered precursors deposited from elemental targets. The crystallization of the V_2AlC MAX phase structure starts from ~560°C and the V_2AlC MAX phase films consist of elongated crystallites parallel to the film/substrate interface because of the multilayered arrangement of the precursors and lateral growth of crystallites during thermal annealing. Nanostructural investigations reveal undulation growth and preferential incorporation of Ar into amorphous C nanolayers within the multilayered precursors and precipitation of high-density nanoscale Ar-rich regions at grain boundaries after annealing. The Ar-rich regions or bubbles display pronounced layered distribution characteristics especially adjacent to the substrate/film interface, and their layered distribution was gradually interrupted due to progressively enhanced undulation growth of subsequently deposited multilayers. These observations suggest that substantially different levels of Ar atoms can be incorporated into the sublayers of multilayered films leading to its layered distribution during deposition. How and to what extent the precipitation of these layered nanoscale Ar-rich regions or bubbles affects the multilayered film's physical and mechanical properties remains to be explored.

Acknowledgements

C. Tang acknowledges financial support by Deutsche Forschungsgemeinschaft (DFG – German Research Foundation, TA 1693/1-1). The authors thank Klaus Seemann and Vincent Otto for supporting the HTXRD measurements.

References

[1] M.W. Barsoum, The MN+1AXN phases: a new class of solids; thermodynamically stable nanolaminates, Prog. Solid State Chem. 28 (2000) 201–281. https://doi.org/10.1016/S0079-6786(00)00006-6.

[2] Z.M. Sun, Progress in research and development on MAX phases: a family of layered ternary compounds, Int. Mater. Rev. 56 (2011) 143–166. https://doi.org/10.1179/1743280410Y.0000000001.

[3] P. Eklund, M. Beckers, U. Jansson, H. Högberg, L. Hultman, The Mn+1AXn phases: Materials science and thin-film processing, Thin Solid Films. 518 (2010) 1851–1878. https://doi.org/10.1016/j.tsf.2009.07.184.

[4] A.S. Ingason, A. Petruhins, J. Rosen, Toward Structural Optimization of MAX Phases as Epitaxial Thin Films, Mater. Res. Lett. 4 (2016) 152–160. https://doi.org/10.1080/21663831.2016.1157525.

[5] J.P. Palmquist, U. Jansson, T. Seppänen, P.O.Å. Persson, J. Birch, L. Hultman, P. Isberg, Magnetron sputtered epitaxial single-phase Ti3SiC2 thin films, Appl. Phys. Lett. 81 (2002) 835–837. https://doi.org/10.1063/1.1494865.

[6] O. Wilhelmsson, P. Eklund, H. Högberg, L. Hultman, U. Jansson, Structural, electrical and mechanical characterization of magnetron-sputtered V-Ge-C thin films, Acta Mater. 56 (2008) 2563–2569. https://doi.org/10.1016/j.actamat.2008.01.036.

[7] H. Rueß, J. Werner, Y. Unutulmazsoy, J.W. Gerlach, X. Chen, B. Stelzer, D. Music, S. Kolozsvari, P. Polcik, T.E. Weirich, J.M. Schneider, Effect of target peak power density on the phase formation, microstructure evolution, and mechanical properties of Cr2AlC MAX-phase coatings, J. Eur. Ceram. Soc. 41 (2021) 1841–1847. https://doi.org/10.1016/j.jeurceramsoc.2020.10.072.

[8] J. Wang, R. Shu, Y. Dong, T. Shao, Q.H. Deng, X.B. Zhou, F. Huang, S.Y. Du, Z.G. Wang, J.M. Xue, Y.G. Wang, Q. Huang, Microstructure evolution of V2AlC coating on Zr substrate under He irradiation and their mechanical behavior, Scr. Mater. 137 (2017) 13–17. https://doi.org/10.1016/j.scriptamat.2017.05.003.

[9] Z. Wang, J. Liu, L. Wang, X. Li, P. Ke, A. Wang, Dense and high-stability Ti2AlN MAX phase coatings prepared by the combined cathodic arc/sputter technique, Appl. Surf. Sci. 396 (2017) 1435–1442. https://doi.org/10.1016/j.apsusc.2016.11.183.

[10] C. Tang, M. Steinbrück, M. Klimenkov, U. Jäntsch, H.J. Seifert, S. Ulrich, M. Stüber, Textured growth of polycrystalline MAX phase carbide coatings via thermal annealing of M/C/Al multilayers, J. Vac. Sci. Technol. A. 38 (2020) 013401. https://doi.org/10.1116/1.5131544.

[11] C. Tang, M. Klimenkov, U. Jaentsch, H. Leiste, M. Rinke, S. Ulrich, M. Steinbrück, H.J. Seifert, M. Stueber, Synthesis and characterization of Ti2AlC coatings by magnetron sputtering from three elemental targets and ex-situ annealing, Surf. Coat. Technol. 309 (2017) 445–455. https://doi.org/10.1016/j.surfcoat.2016.11.090.

[12] A. V. Pshyk, E. Coy, M. Kempiński, B. Scheibe, S. Jurga, Low-temperature growth of epitaxial Ti2AlC MAX phase thin films by low-rate layer-by-layer PVD, Mater. Res. Lett. 7 (2019) 244–250.

https://doi.org/10.1080/21663831.2019.1594428.

[13] C. Torres, R. Quispe, N.Z. Calderón, L. Eggert, M. Hopfeld, C. Rojas, M.K. Camargo, A. Bund, P. Schaaf, R. Grieseler, Development of the phase composition and the properties of Ti_2AlC and Ti_3AlC_2 MAX-phase thin films – A multilayer approach towards high phase purity, Appl. Surf. Sci. 537 (2021) 147864. https://doi.org/10.1016/j.apsusc.2020.147864.

[14] M. Stevens, H. Pazniak, A. Jemiola, M. Felek, M. Farle, U. Wiedwald, Pulsed laser deposition of epitaxial Cr_2AlC MAX phase thin films on MgO(111) and Al_2O_3(0001), Mater. Res. Lett. 9 (2021) 343–349. https://doi.org/10.1080/21663831.2021.1920510.

[15] K. Thompson, D. Lawrence, D.J. Larson, J.D. Olson, T.F. Kelly, B. Gorman, In situ site-specific specimen preparation for atom probe tomography, Ultramicroscopy. 107 (2007) 131–139. https://doi.org/10.1016/j.ultramic.2006.06.008.

[16] Y. Jiang, R. Iskandar, M. to Baben, T. Takahashi, J. Zhang, J. Emmerlich, J. Mayer, C. Polzer, P. Polcik, J.M. Schneider, Growth and thermal stability of $(V,Al)_2C_x$ thin films, J. Mater. Res. 27 (2012) 2511–2519. https://doi.org/10.1557/jmr.2012.202.

[17] A. Abdulkadhim, M. To Baben, V. Schnabel, M. Hans, N. Thieme, C. Polzer, P. Polcik, J.M. Schneider, Crystallization kinetics of V_2AlC, Thin Solid Films. 520 (2012) 1930–1933. https://doi.org/10.1016/j.tsf.2011.09.037.

[18] N. Bahlawane, D. Lenoble, Vanadium oxide compounds: Structure, properties, and growth from the gas phase, Chem. Vap. Depos. 20 (2014) 299–311. https://doi.org/10.1002/cvde.201400057.

[19] C. Azina, S. Mráz, G. Greczynski, M. Hans, D. Primetzhofer, J.M. Schneider, P. Eklund, Oxidation behaviour of V_2AlC MAX phase coatings, J. Eur. Ceram. Soc. 40 (2020) 4436–4444. https://doi.org/10.1016/j.jeurceramsoc.2020.05.080.

[20] J.J. Li, L.F. Hu, F.Z. Li, M.S. Li, Y.C. Zhou, Variation of microstructure and composition of the Cr_2AlC coating prepared by sputtering at 370 and 500 °C, Surf. Coat. Technol. 204 (2010) 3838–3845. https://doi.org/10.1016/j.surfcoat.2010.04.067.

[21] J. Rosen, P.O.Å. Persson, M. Ionescu, A. Kondyurin, D.R. McKenzie, M.M.M. Bilek, Oxygen incorporation in Ti_2AlC thin films, Appl. Phys. Lett. 92 (2008) 064102. https://doi.org/10.1063/1.2838456.

[22] M. Baben, L. Shang, J. Emmerlich, J.M. Schneider, Oxygen incorporation in M_2AlC (M = Ti, V, Cr), Acta Mater. 60 (2012) 4810–4818. https://doi.org/10.1016/j.actamat.2012.05.011.

[23] M. Herbig, D. Raabe, Y.J. Li, P. Choi, S. Zaefferer, S. Goto, Atomic-scale quantification of grain boundary segregation in nanocrystalline material, Phys. Rev. Lett. 112 (2013) 1–5. https://doi.org/10.1103/PhysRevLett.112.126103.

[24] X. Chen, B. Stelzer, M. Hans, R. Iskandar, J. Mayer, J.M. Schneider, Enhancing the high temperature oxidation behavior of Cr_2AlC coatings by reducing grain boundary nanoporosity, Mater. Res. Lett. 9 (2021) 127–133. https://doi.org/10.1080/21663831.2020.1854358.

[25] Z. Gao, X. Zhang, J. Kulczyk-Malecka, Y. Chen, E. Bousser, P. Kelly, P. Xiao, Ceramic buckling for determining the residual stress in thin films, Scr. Mater. 201 (2021) 113949. https://doi.org/10.1016/j.scriptamat.2021.113949.

[26] G. Abadias, E. Chason, J. Keckes, M. Sebastiani, G.B. Thompson, E. Barthel, G.L. Doll, C.E. Murray, C.H. Stoessel, L. Martinu, Review Article: Stress in thin films and coatings: Current status, challenges, and prospects, J. Vac. Sci. Technol. A Vacuum, Surfaces, Film. 36 (2018) 020801. https://doi.org/10.1116/1.5011790.

[27] A. Moridi, H. Ruan, L.C. Zhang, M. Liu, Residual stresses in thin film systems: Effects of lattice mismatch, thermal mismatch and interface dislocations, Int. J. Solids Struct. 50 (2013) 3562–3569. https://doi.org/10.1016/j.ijsolstr.2013.06.022.

[28] W.W.Y. Lee, D. Oblas, Argon entrapment in metal films by dc triode sputtering, J. Appl. Phys. 46 (1975) 1728–1732. https://doi.org/10.1063/1.321776.

[29] H.F. Winters, E. Kay, Gas incorporation into sputtered films, J. Appl. Phys. 38 (1967) 3928–3934. https://doi.org/10.1063/1.1709043.

[30] L. Hultman, J. -E. Sundgren, L.C. Markert, J.E. Greene, Ar and excess N incorporation in epitaxial TiN films grown by reactive bias sputtering in mixed Ar/N 2 and pure N 2 discharges , J. Vac. Sci. Technol. A Vacuum, Surfaces, Film. 7 (1989) 1187–1193. https://doi.org/10.1116/1.576251.

[31] S. Gleich, R. Soler, H. Fager, H. Bolvardi, J.O. Achenbach, M. Hans, D. Primetzhofer, J.M. Schneider, G. Dehm, C. Scheu, Modifying the nanostructure and the mechanical properties of Mo2BC hard coatings: Influence of substrate temperature during magnetron sputtering, Mater. Des. 142 (2018) 203–211. https://doi.org/10.1016/j.matdes.2018.01.029.

[32] J. Schwan, S. Ulrich, H. Roth, H. Ehrhardt, S.R.P. Silva, J. Robertson, R. Samlenski, R. Brenn, Tetrahedral amorphous carbon films prepared by magnetron sputtering and dc ion plating, J. Appl. Phys. 79 (1996) 1416–1422. https://doi.org/10.1063/1.360979.

[33] Y.P. Chien, S. Mráz, M. Fekete, M. Hans, D. Primetzhofer, S. Kolozsvári, P. Polcik, J.M. Schneider, Deviations between film and target compositions induced by backscattered Ar during sputtering from M2-Al-C (M = Cr, Zr, and Hf) composite targets, Surf. Coat. Technol. 446 (2022). https://doi.org/10.1016/j.surfcoat.2022.128764.

[34] C.C. Fang, F. Jones, R.R. Kola, G.K. Celler, V. Prasad, Stress and microstructure of sputter-deposited thin films: Molecular dynamics simulations and experiment, J. Vac. Sci. Technol. B Microelectron. Nanom. Struct. 11 (1993) 2947. https://doi.org/10.1116/1.586566.

[35] T. Itoh, N. Mutsukura, Mechanical properties of a-C:H thin films deposited by r.f. PECVD method, Vacuum. 77 (2004) 11–18. https://doi.org/10.1016/j.vacuum.2004.07.065.

[36] J. Nomoto, T. Nakajima, I. Yamaguchi, T. Tsuchiya, Influence of unintentionally incorporated Ar atoms on the crystalline polarity of magnetron-sputtered Al-doped ZnO polycrystalline films on glass and sapphire substrates, J. Vac. Sci. Technol. B. 38 (2020) 022202. https://doi.org/10.1116/1.5129684.

[37] D. Raabe, M. Herbig, S. Sandlöbes, Y. Li, D. Tytko, M. Kuzmina, D. Ponge, P.P. Choi, Grain boundary segregation engineering in metallic alloys: A pathway to the design of interfaces, Curr. Opin. Solid State Mater. Sci. 18 (2014) 253–261. https://doi.org/10.1016/j.cossms.2014.06.002.

[38] M. Stueber, H. Holleck, H. Leiste, K. Seemann, S. Ulrich, C. Ziebert, Concepts for the design of advanced nanoscale PVD multilayer protective thin films, J. Alloys Compd. 483 (2009) 321–333. https://doi.org/10.1016/j.jallcom.2008.08.133.

[39] G. Greczynski, I. Petrov, J.E. Greene, L. Hultman, Paradigm shift in thin-film growth by magnetron sputtering: From gas-ion to metal-ion irradiation of the growing film, J. Vac. Sci. Technol. A. 37 (2019) 060801. https://doi.org/10.1116/1.5121226.